Egypt. J. Chem. **Vol. 68**, No. 4, pp. 37 - 52 (2025)

Egyptian Journal of Chemistry

http://ejchem.journals.ekb.eg/

A comparative study of stainless steel 310 and N350 in high temperature oxidation

Esraa Kamel[a], Sanaa S. Abd ElMoamen[b], Emad El-Kashif[a], Lamiaa Z. Mohamed[c,*]

[a] *Department of Mechanical Design and Production - Faculty of Engineering, Cairo University, Giza, 12613, Egypt.*
[b] *Tabbin Institute for Metallurgical Studies, P.O. Box 11421, Helwan, Egypt*
[c] *Mining, Petroleum and Metallurgical Engineering Department, Faculty of Engineering, Cairo University, Giza, 12613, Egypt.*

Abstract

A comparison study was conducted to investigate the chemical, physical, and mechanical properties of N350 and stainless steel 310 (SS 310). According to the findings, N350 has an average hardness that is twice as high as SS310. The microstructure and phase identification were examined using optical microscopy (OM) and scanning electron microscopy (SEM), while the chemical composition was examined by energy dispersive x-ray analysis (EDX) and x-ray diffraction (XRD). The value of Young's modulus of N350 is higher than that of SS310. The oxidation kinetics of the SS310 and N350 were demonstrated at 850, 950, and 1050 °C in dry air for 50 h. The oxidation kinetics for both SS310 and N350 follow the parabolic law. The parabolic constants of SS310 are $3.00x10^{-9}$ $g^2/(cm^4 \cdot h)$, $2.00x10^{-8}$ $g^2/(cm^4 \cdot h)$, $2.00x10^{-6}$ $g^2/(cm^4 \cdot h)$ for 850 °C, 950 °C, and 1050 °C, respectively. While the parabolic constants of N350 are $7.00x10^{-9}$ $g^2/(cm^4 \cdot h)$, $9.00x10^{-6}$ $g^2/(cm^4 \cdot h)$, and $2.00x10^{-5}$ $g^2/(cm^4 \cdot h)$ for 850 °C, 950 °C, and 1050 °C, respectively. The activation energy of N350 (217.6 KJ/mol) is higher than that of SS310 (172.05 KJ/mol). The surface structure, elemental composition, and phase characterization of the samples under various oxidation conditions were analyzed using SEM, EDX, and XRD techniques after 50 h. The findings indicate that N350 steel is more suitable for use in the glass mold industry than SS310 steel.

Keywords: High temperature oxidation; Glass mold dies; 310 stainless steel; N350 stainless steel; Microstructure

1. Introduction

The glass molding process (GMP) is gaining popularity as an alternative to traditional glass material production methods, offering advantages such as precise forming, a short production cycle, cost-effectiveness, and environmental friendliness [1, 2]. Stainless steel (SS) finds primary use in industry, automobiles, trucks, and freight cars, with alloys containing Ni, Cr, and Mg for corrosion resistance and cost efficiency [3, 4]. Advances in ultra-supercritical thermal power and nuclear power technologies drive the employment of the austenitic stainless steels (ASSs) not only in low temperature environments but also increasingly in high temperature settings. Specifically, ASS is gaining prominence as a critical component in high temperature conditions. Consequently, investigating the oxidation resistance of ASSs becomes crucial for practical engineering applications [5]. To attain oxidation resistance at elevated temperatures, ASSs form a stable, dense, and solid oxide protection scale. In high-temperature operations, common scales for ASSs containing elements like Mn and Cr include Cr_2O_3, Mn_2O_3, and others [6].

Various industries, including automobiles, energy, and home appliances, widely employ ferritic SSs due to their outstanding high-temperature oxidation resistance, corrosion resistance, cost-effectiveness, minimal thermal expansion coefficient, and high thermal conductivity. This makes it a preferred choice as an energy-efficient and environmentally friendly SS material [7, 8]. The resistance to high-temperature oxidation is a crucial parameter for assessing SS performance in elevated-temperature applications [9, 10]. Different chemical compositions in ferritic SSs produce distinct oxidation products and oxide

*Corresponding author e-mail: lamiaa.zaky@cu.edu.eg ; (Lamiaa Z. Mohamed).
Receive Date: 10 July 2024, Revise Date: 07 August 2024, Accept Date: 18 August 2024
DOI: 10.21608/ejchem.2024.303345.9987

film structures, resulting in a variety of high-temperature failure origins. Recent research efforts by material scientists have delved into the oxidation behavior of SSs.

Vicente et. al. [11] guided an investigation on the oxidation kinetics of EN1.4509 ferritic SS at elevated temperatures for varying durations. Comparison of surface morphologies after oxidation for 8 minutes and 24 h revealed octahedral-shaped oxidation products, with particle size increasing over time. The investigation also assessed the growth kinetics and composition of the oxide film developed following short-term oxidation at various temperatures. Results indicated that the oxide film primarily comprised Cr at 850 °C for 2 h, transitioning to Fe above 900 °C. The oxidation rate exhibited a positive correlation with temperature and the Ni, Fe, and Cr content in the alloy [12, 13]. Notably, the formation of Cr_2O_3 and Fe-Cr spinel compounds at high temperatures by alloys containing Cr greatly improved their resistance to oxidation. These compounds elevated the activation energy required for metal ion diffusion, thereby retarding the diffusion rate at the interface. Consequently, this slowed down oxide scale growth and bolstered the steel's resistance to oxidation [14, 15]. While current research on Cr-containing steels predominantly concentrates on conventional structural and SSs characterized by low Cr content, there remains a scarcity of exploration into high-temperature oxidation in Cr-containing steel categories beyond these conventional types [16].

Stainless Steel 310 (SS310) stands out as an ASS alloy recognized for its remarkable resistance to high-temperature oxidation. Notably, the 310S SS variant possesses elevated Cr and Ni contents in comparison to the frequently cited SS304L/SS316L. The higher Cr content plays a critical role in fostering the development of a protective surface oxide film, while the increased Ni content contributes to enhancing the oxide film's stability [17, 18]. The N350 is a ferritic SS with high temperature oxidation resistance. Industrial applications often use both SS310 and the N350, both high-temperature alloys, for their resistance to oxidation at elevated temperatures. When exposed to elevated temperatures in dry air, SS310 forms a protective Cr_2O_3 layer on the surface [19]. This layer enhances the material's resistance to further oxidation. SS310 can withstand temperatures well up to 1000°C, which is beneficial for applications in various industrial processes, including glass manufacturing. Glass manufacturing processes often involve high temperatures. Both SS310 and N350 should be selected based on their ability to maintain mechanical properties and resist oxidation at the operating temperatures of the glass manufacturing process. The formation of a protective oxide layer is critical for preventing the material's degradation. Regular maintenance and appropriate heat treatment processes can help maintain the protective oxide layer. The paramount quality for SS to be utilized in the glass molding process is its high-temperature oxidation resistance. The development of separate oxide layers on SS surfaces depends on various factors, including alloy composition and specific oxidizing conditions such as temperature, atmosphere, and duration of oxidation [20].

The objective of this study was to examine the mechanical, physical, and chemical properties of both N350 and SS310. The microstructure and phase identification of the two types of steels were examined using optical microscopy (OM), scanning electron microscopy (SEM), composition by energy dispersive x-ray analysis (EDX), and x-ray diffraction (XRD). Hardness and Young's modulus were investigated for the SS310 and N350. The oxidation behavior of the SS310 and N350 was examined at 850, 950, and 1050 °C in dry air for 50 h. The surface morphology, elemental analysis, and phase identification of the investigated samples after oxidation in all conditions after 50 h were examined using SEM, EDX, and XRD, respectively.

1. Experimental work

2.1 Stainless steel characteristics

Table 1 lists the chemical analyses performed on SS310 and N350. The investigated alloys were prepared for microstructure examination by grinding with emery papers till 1000 grit then polishing with alumina paste 0.3 μm. The polished samples were etched with 10% HNO_3, and 10% HCl and the rest was distilled water. The microstructure is done by using the optical microscopy (OM) model Zeiss Axiotech 30 and scanning electron microscopy (SEM) model (FEI inspect S-Netherlands) where the elemental analysis using the energy dispersive X-ray analysis (EDX) attached SEM model (Bruker AXS-flash detector Germany). The phase identification is done by the x-ray diffraction (XRD) analysis utilizing the X'Pert PRO PAN analytical diffractometer, with a Cu Kα radiation source of λ = 0.15406 nm, operating at 45 kV and 40 mA.

Table 1. Chemical analysis of both SS310 and N350.

Alloys	Element, wt. %								
	C	Si	Mn	Cr	Ni	Mo	Cu	V	Fe
SS310	0.04	0.42	1.64	25.06	20.28	0.15	0.29	0.06	Bal.
N350	0.22	0.29	0.45	15.95	1.63	0.11	0.06	0.05	Bal.

The Vickers hardness values use the device model Zwick/Roell (ZHU250). The hardness test was measured using a load of 10 kg with 5 reads for each alloy to calculate the average values. The Young's modulus device employs a physical method to measure the Ultrasonic Flaw Detector (USM3) model. It uses a sensitivity balance (Mettler H 72 model) with a capacity of 160 g and a readability of 0.1 mg. The following equations are used in the calculations of different parameters exerted from the test [21]:

$$L = \rho v_l^2 \quad (1)$$

$$G = \rho v_s^2 \quad (2)$$

$$K = L - (4/3)\, G \quad (3)$$

$$E = 2(1+\sigma)\, G \quad (4)$$

$$\sigma = (L-2G)/2(L-G) \quad (5)$$

Where L donates longitudinal modulus, G represents shear modulus, K indicates bulk modulus, E is Young's modulus, and σ is Poisson's ratio.

2.2 Oxidation

The specimens from both alloys were cut into dimensions of 1 cm x 1 cm for the oxidation test. The oxidation behavior of SS310 and N350 was observed at temperatures of 850, 950, and 1050 °C over a time range spanning 10 to 50 h in dry air at a flow rate of 2 liters per minute. A vertical tube furnace, specifically the EVA 12/300B model by CARBOLITE GERO, was employed for this experimentation. The "version programmer 3216 P5" computer program controlled the oxidation process. During the oxidation period, mass changes were monitored using a high-precision electrical balance (METTLER-TOLEDO Model MS 204 S/01) at 10 h intervals. X-ray Diffraction (XRD) was employed to investigate the phases of the oxide layer. Subsequently, the oxidized samples were subjected to Scanning Electron Microscopy (SEM) and Energy Dispersive X-ray analysis (EDX) to elucidate surface morphology and elemental composition after 50 h for the respective temperatures.

2. Results and discussion

3.1 Stainless steel properties

Fig. 1 illustrates the optical microstructures of SS310 and N350. Additionally, Fig. 2 presents the SEM images of the two investigated alloys. The spot EDX analysis for SS310 exists in Fig. 3, whereas the spot EDX analysis for N350 is presented in Fig. 4.

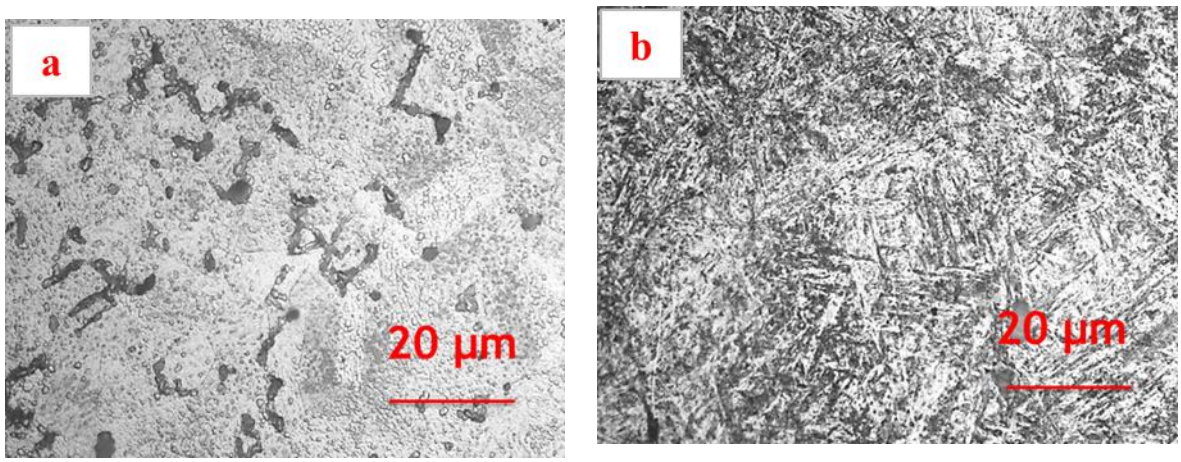

Fig. 1. The optical microstructure of (a) SS310, and (b) N350.

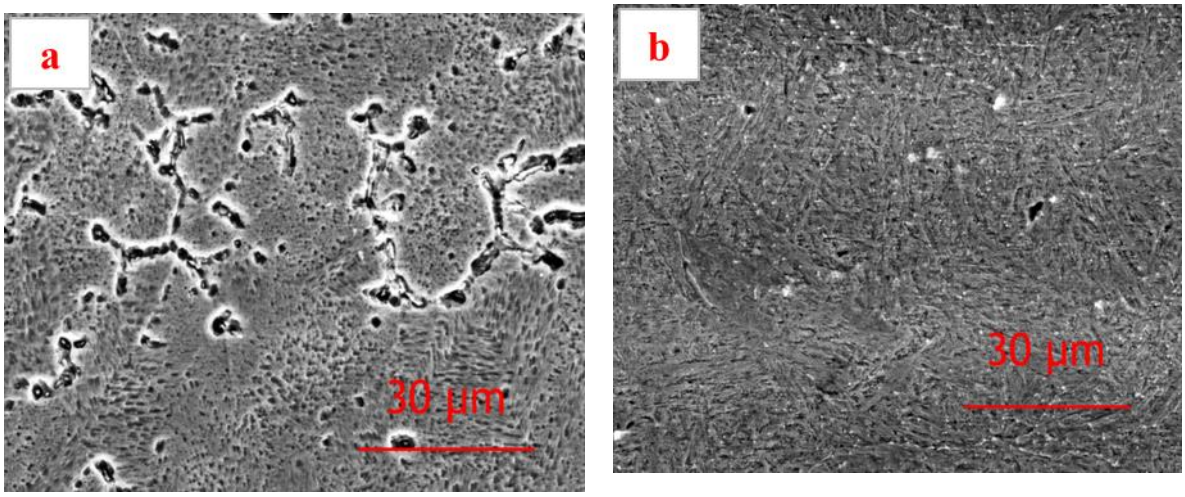

Fig. 2. The SEM micrographs of (a) SS310, and (b) N350.

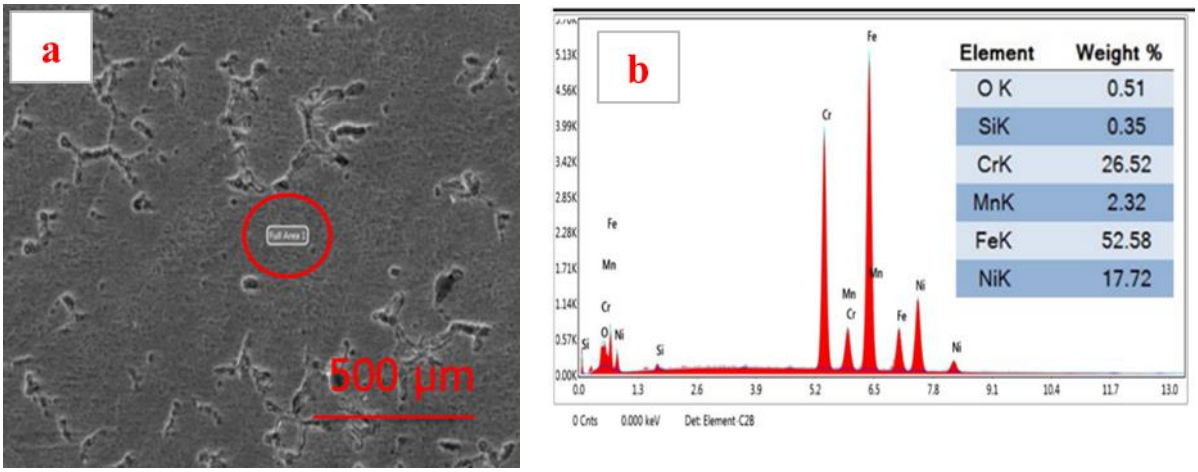

Fig. 3. The SEM micrograph and EDX result of SS310.

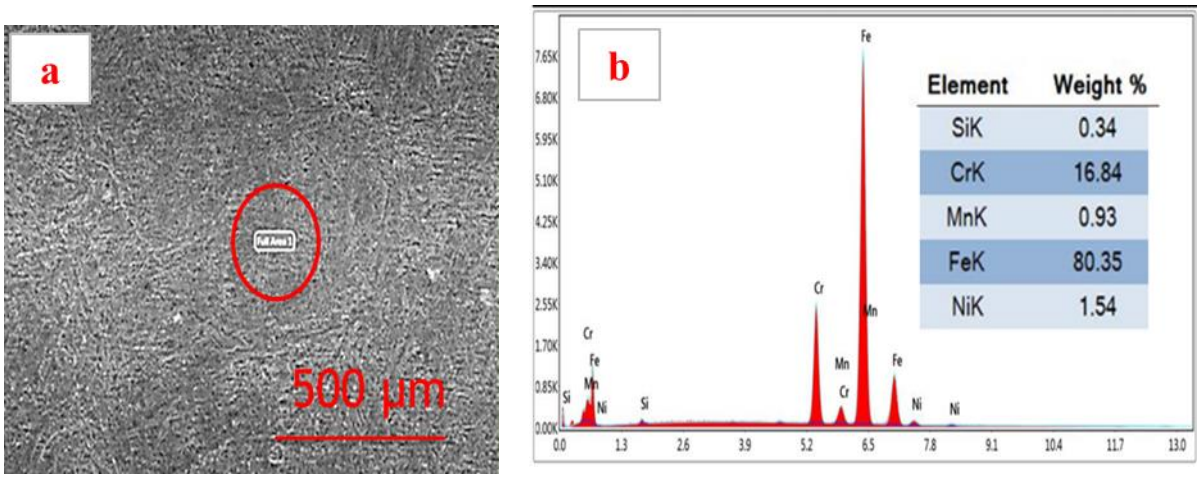

Fig. 4. The SEM micrograph and EDX result of N350.

Before oxidation, the XRD pattern of SS310 has iron phase (COD 9008469) and austenite phase (PDF 00-052-0512), while the XRD pattern of N350 has iron phase (COD 9008469) as seen in Fig. 5.

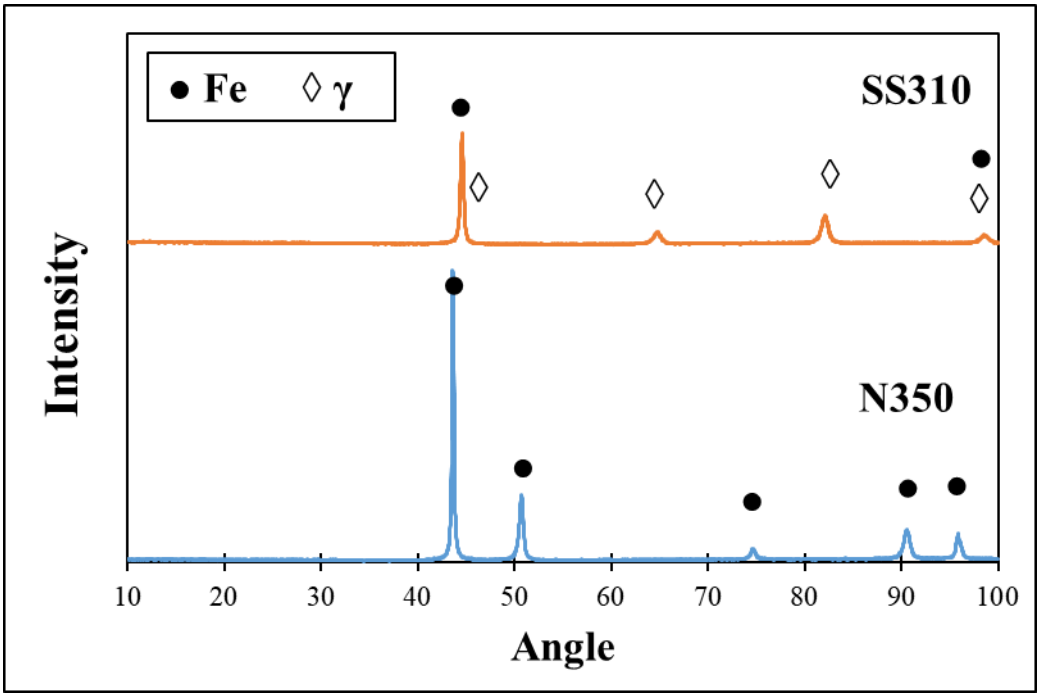

Fig. 5. The XRD patterns of SS310 and N350.

Hardness

The average Vickers hardness values are given in Fig. 6. The hardness of the N350 (418 HV) is about twice the hardness of the SS310 (200 HV), as shown in Fig. 6.

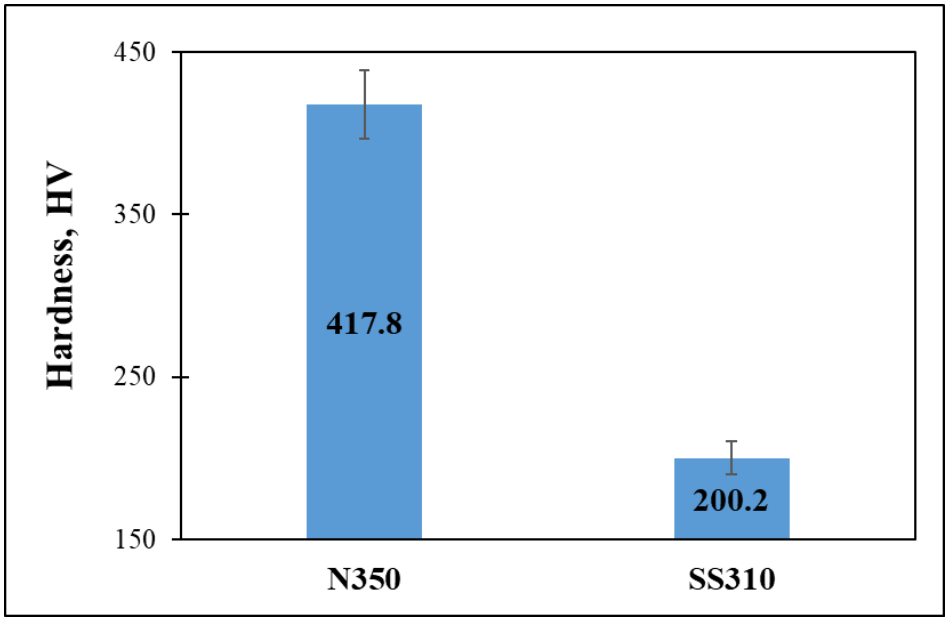

Fig. 6. The hardness values of SS310 and N350.

Youngs modulus

Fig. 7 presents the Young's modulus values. The Youngs modulus of the N350 (219 Gpa) is higher than the Youngs modulus for the SS310 (194 Gpa). This result is consistent with the hardness results above.

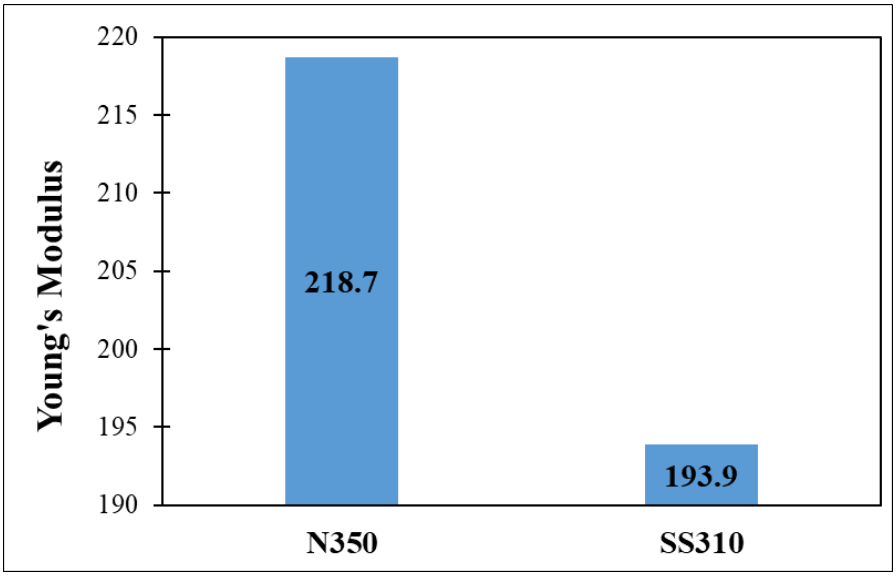

Fig. 7. The Young's modulus values of SS310 and N350

3.2. Oxidation kinetics

Figs. 8 and 9 depict the weight gain per unit area versus oxidation times for SS310 and N350, respectively, at temperatures of 850, 950, and 1050 °C. The weight gain curves presented in these figures highlight distinct oxidation behaviors exhibited by the alloys at different temperatures and durations. In Fig. 8, it is evident that at 850 °C, there is a marginal increase in weight gain with prolonged oxidation times, while at 950 °C, the weight gain shows a gradual rise. However, at 1050 °C, weight gain increases significantly over time. Fig. 9 shows a similar trend, with a slight increase in weight gain at 850 °C and a substantial increase at both 950 °C and 1050 °C as time increases. In summary, Eq. (6) represents the high-temperature oxidation kinetics [22, 23, 24].

$$(\Delta W / \Delta A)^n = k_p t \quad (6)$$

Where ΔW represents the weight gain per unit area, Kp denotes the parabolic rate constant, t stands for the oxidation time, and n signifies the rate exponent.

The value of n is approximately 2, indicating that the oxidation kinetics of SS310 and N350 follow a parabolic pattern. The oxidation rate constant, Kp, can be derived by plotting $(\Delta W/A)^2$ against t, as illustrated in Figs 10 and 11. Their findings reveal that the rate constant, Kp, for both SS310 and N350, escalates with rising temperatures. Consequently, the oxidation kinetics adhere to the parabolic law for SS310 and N350. The parabolic rate constant values of SS310 are $3.00\text{x}10^{-9}$ $g^2/(cm^4 \cdot h)$, $2.00\text{x}10^{-8}$ $g^2/(cm^4 \cdot h)$, $2.00\text{x}10^{-6}$ $g^2/(cm^4 \cdot h)$ for 850 °C, 950 °C, and 1050 °C, respectively. While the parabolic constants of N350 are $7.00\text{x}10^{-9}$ $g^2/(cm^4 \cdot h)$, $9.00\text{x}10^{-6}$ $g^2/(cm^4 \cdot h)$, and $2.00\text{x}10^{-5}$ $g^2/(cm^4 \cdot h)$ for 850 °C, 950 °C, and 1050 °C, respectively. The oxidation rate values increase with increased oxidation temperature for both the SS310 and N350. This may be due to the increase of Cr content in SS310, which contains a protective layer of Cr_2O_3 till 1000 °C, then it begins to volatile as CrO reduces the oxidation resistance.

Plotting log Kp against 1/T can determine the activation energy of N350 and SS310 alloys, as shown in Figs. 12 and 13. Following the Arrhenius equation, the linear relationship conforms to the formula in Eq. (7) [25, 26, 27].

$$Kp = A \exp(-Q/RT) \quad (7)$$

In the equation, A represents the model constant, Q signifies the activation energy of the alloy (J/mol), T denotes the oxidation temperature (K), and R stands for the gas constant (8.314 J/(mol·K)).

Hence, the activation energy for the oxidation process of N350 and SS310 within the temperature range of 850-1050°C for 50 h in dry air amounts to 217.6 kJ/mol and 172 kJ/mol, respectively. Consequently, it can be inferred that the oxidation resistance of N350 surpasses that of SS310 under the analyzed conditions. This may be due to the decrease in the Cr content of N350 than that of SS310, which decreases the phenomenon of Cr depletion and volatilization at high temperatures [28].

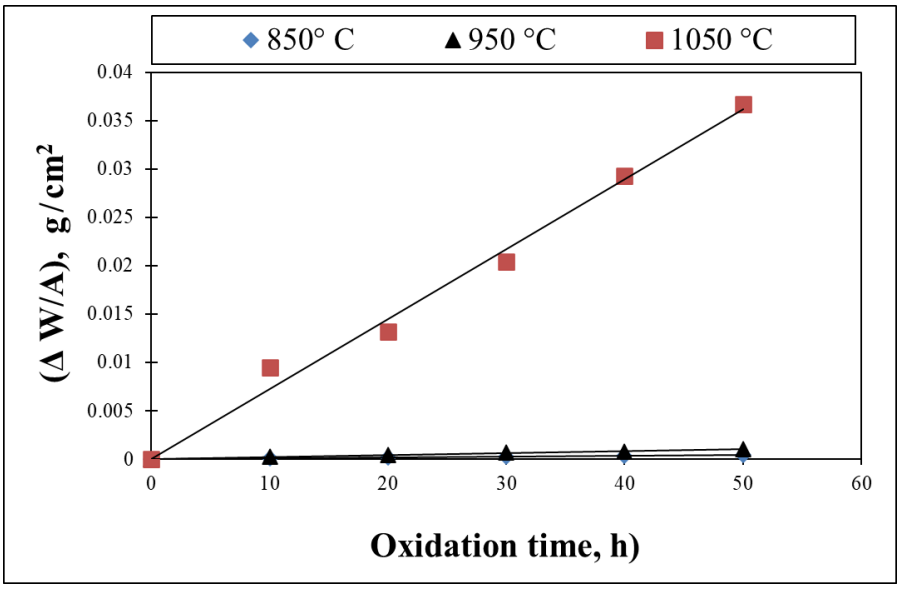

Fig. 8. The change in (ΔW/A) of SS310 against oxidation durations at temperatures of 850°C, 950°C, and 1050°C in a dry air atmosphere.

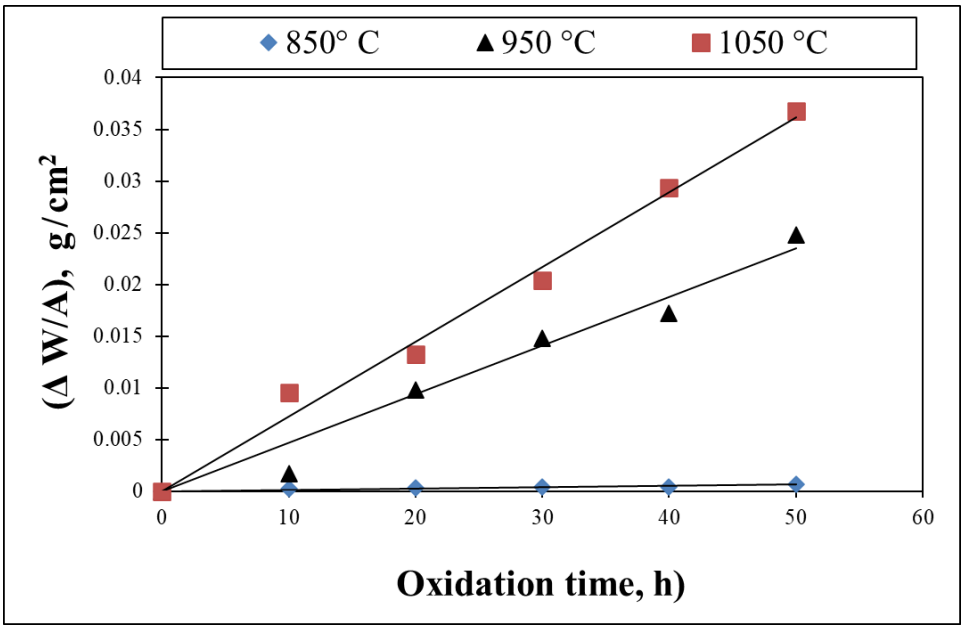

Fig. 9. The change in (ΔW/A) of N350 against oxidation durations at temperatures of 850°C, 950°C, and 1050°C in a dry air atmosphere.

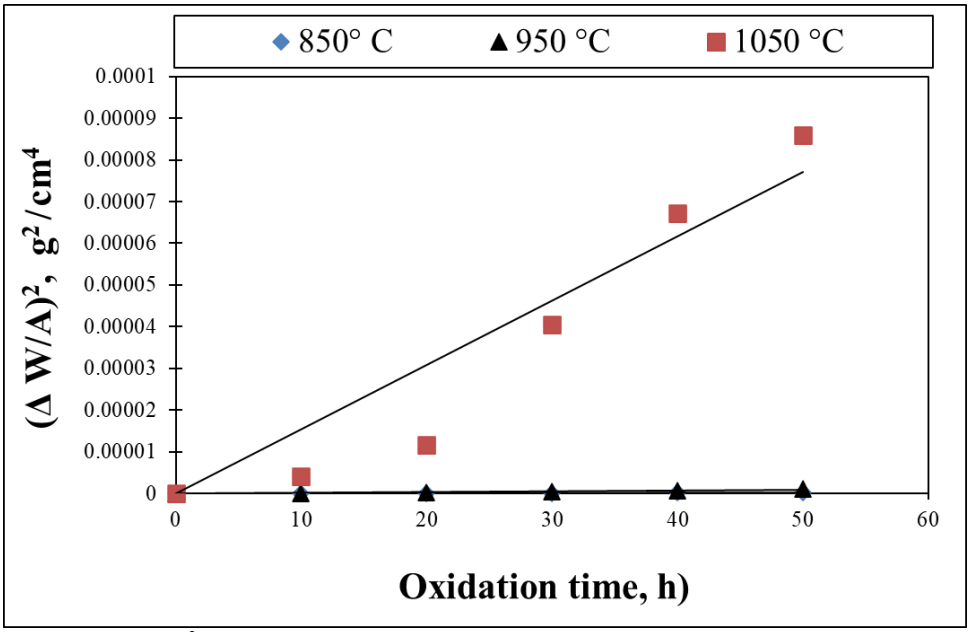

Fig. 10. The change in $(\Delta W/A)^2$ of SS310 against oxidation durations at temperatures of 850°C, 950°C, and 1050°C in a dry air atmosphere.

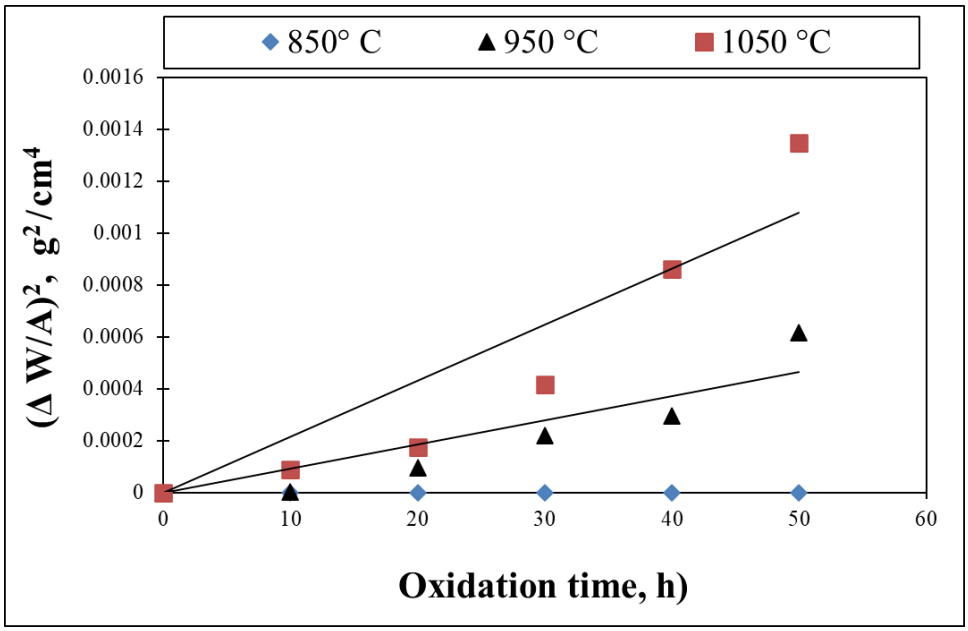

Fig. 11. The change in $(\Delta W/A)^2$ of N350 against oxidation durations at temperatures of 850°C, 950°C, and 1050°C in a dry air atmosphere.

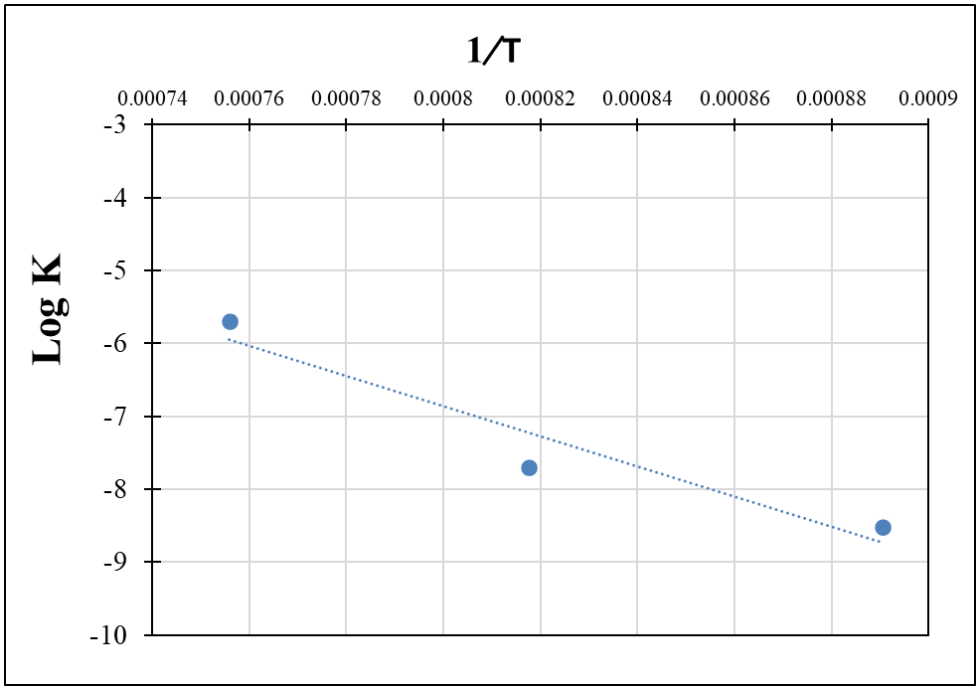

Fig. 12. The Arrhenius plot of the parabolic rate constant for the oxidation of SS310 within the temperature range of 850–1050°C, covering oxidation durations up to 50 h in a dry air environment.

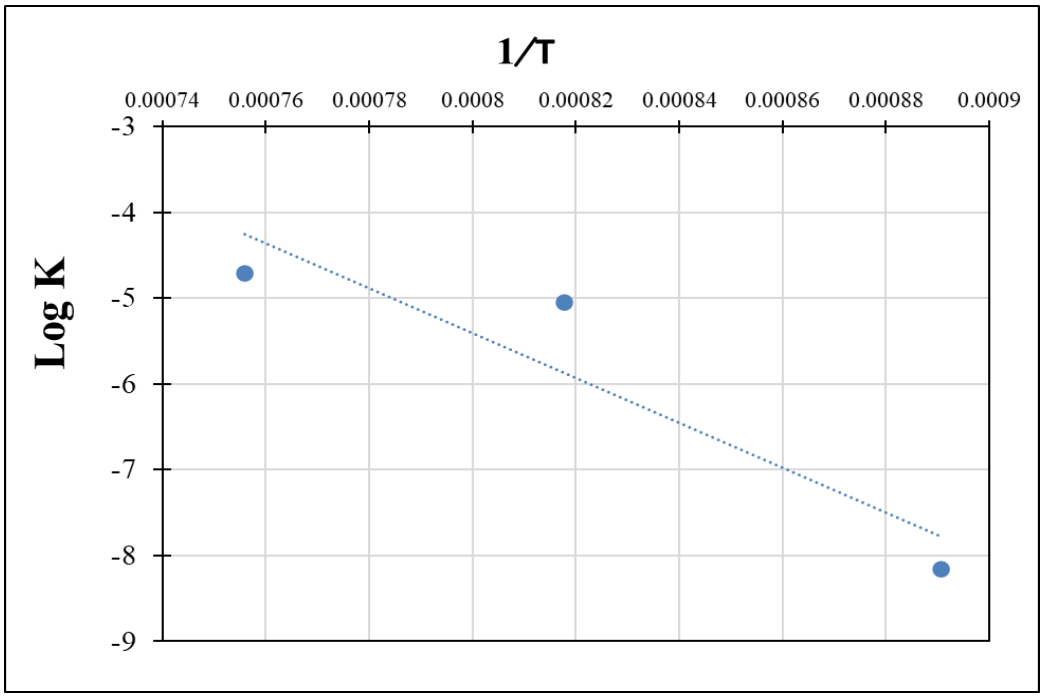

Fig. 13. The Arrhenius plot of the parabolic rate constant for the oxidation of N350 within the temperature range of 850–1050°C, covering oxidation durations up to 50 h in a dry air environment.

The XRD pattern of SS310 after oxidation at temperatures of 850 and 950 °C for 50 h in dry air has iron phase (COD 9008469), Fe_2O_3 phase (PDF 00-013-0534), Fe_3O_4 phase (PDF 01-075-0449), Cr_2O_3 (PDF 38-1479) and a small amount of $FeCr_2O_4$ (JCPDS 24-0512), while austenite phase (PDF 00-052-0512) appears at 950 °C. Finally, the XRD pattern of SS310 at 1050 °C for 50 h has iron phase (COD 9008469), Fe_2O_3 phase (PDF 00-013-0534), and Fe_3O_4 phase (PDF 01-075-0449) as shown in Fig. 14. However, the XRD pattern for N350 after oxidation at oxidation temperatures 850 and 950°C for 50 h has

iron phase (COD 9008469), Fe_2O_3 phase (PDF 00-013-0534), and a small amount of Cr_2O_3 (PDF 38-1479), while Fe_3O_4 phase (PDF 01-075-0449) appears at 950°C. Finally, the XRD pattern for N350 at 1050 °C for 50 h has Fe_2O_3 phase (PDF 00-013-0534), and Fe_3O_4 phase (PDF 01-075-0449) as existed in Fig. 15. Other spinels could exist, but they are not detected by the XRD because they are small amounts, such as $MnFe_2O_4$, $MnCr_2O_4$, and/or $(Fe, Ni, Cr)_xO_y$.

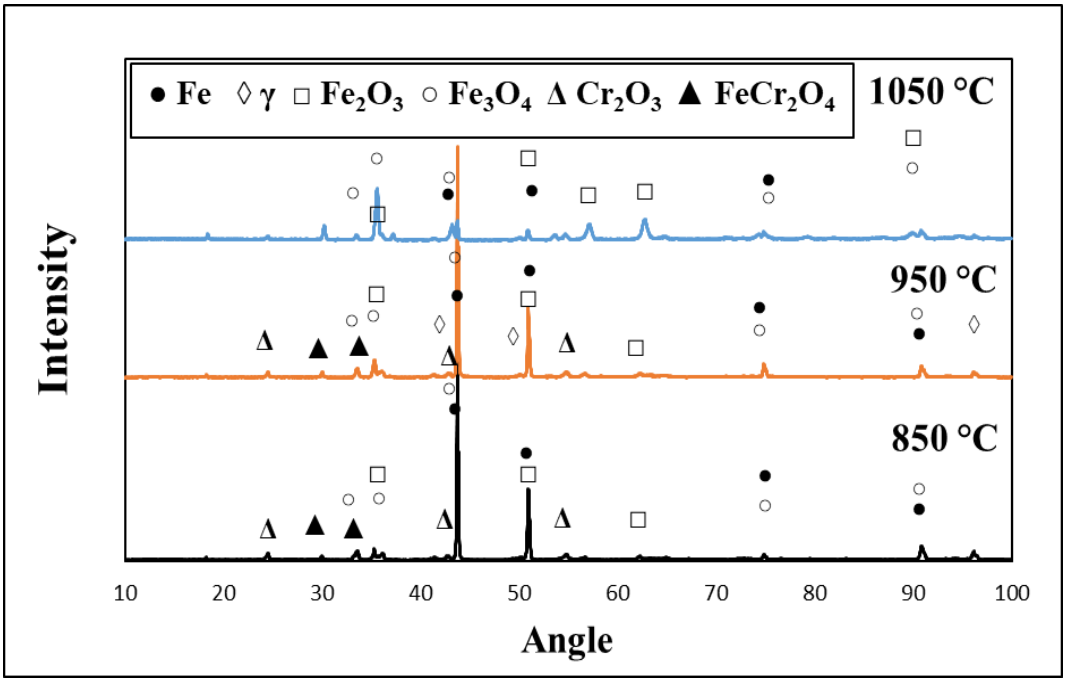

Fig. 14. The XRD results of oxidized SS310 at temperatures of 850°C, 950°C, and 1050°C for a duration of 50 h in a dry air environment.

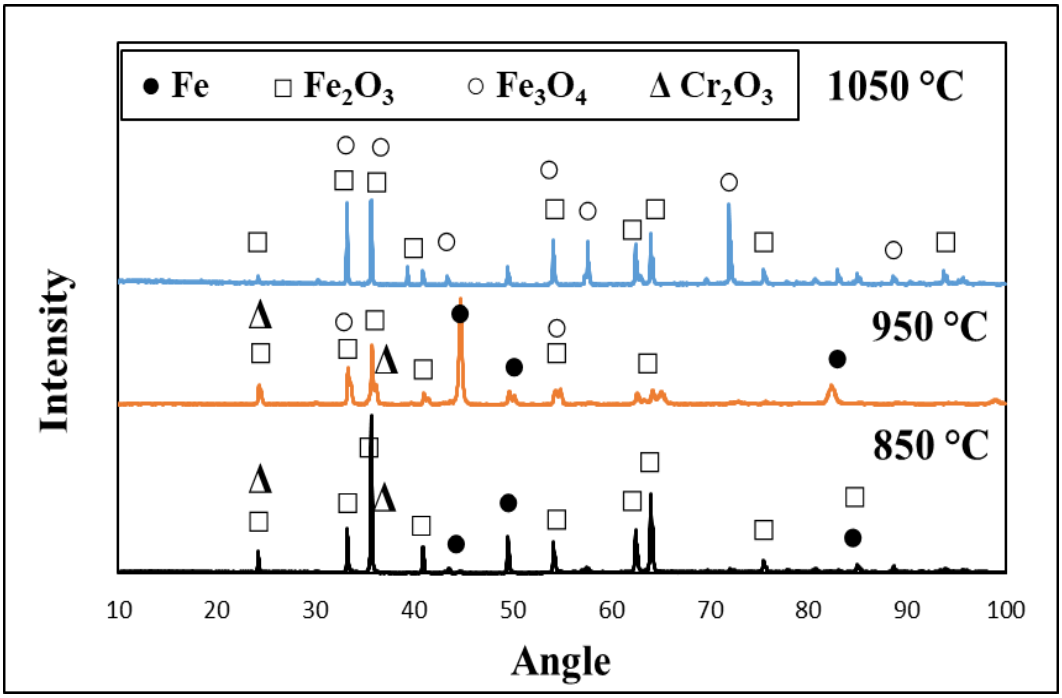

Fig. 15. The XRD results of oxidized N350 at temperatures of 850°C, 950°C, and 1050°C for a duration of 50 h in a dry air environment.

3.3 Surface morphology

Fig. 16 displays surface morphology images of oxidized SS310 after undergoing 50 h of oxidation in dry air at temperatures of 850°C, 950°C, and 1050°C. The SEM images in Figures 16(a and c) show the formation of multilayers of the oxide layers, while Fig. 16(b) shows rhombohedral grains and little messy grains. Fig. 17 showcases the EDX results of oxidized SS310 at various oxidation temperatures for 50 h in dry air. The chromium oxides appear in the EDX results at 850 °C and 950 °C due to the increase in the chromium content which decreases at 1050 °C and the decrease in the oxygen content. It's crucial to highlight that the lack of Cr-oxides at temperatures surpassing 1000°C shouldn't be solely attributed to the volatilization of Cr_2O_3 beyond approximately 1000°C. This is because chromium and manganese tend to form mixed oxides at elevated temperatures, and the presumed volatile CrO_3 isn't stable under such low oxygen partial pressures in the context of this study [29, 30]. The presence of chromium oxide in the external layer is intricately linked to Cr segregation. Increasing the temperature led to a discontinuous layer of chromium oxide. The formation of Cr_2O_3 and spinel $FeCr_2O_4$ is according to the following equations [17]:

$$2Cr + 1.5O_2 \rightarrow Cr_2O_3 \quad (8)$$

$$Cr_2O_3 + Fe + 0.5O_2 \rightarrow FeCr_2O_4 \quad (9)$$

Surface morphology images after oxidation 50 h in dry air of oxidized N350 at 850 °C, 950 °C, and 1050 °C are given in Fig. 18. The SEM images in Fig. 18(a) contain a multi-layer of oxide layers, while Fig. 18(b) shows a cotton shape, and Fig. 18(c) is like a dimple shape. While the EDX analyses of the oxidized N350 at different oxidation temperatures for 50 h in dry air are represented in Fig. 19. Chromium oxides are present at all oxidation temperatures, acting as a protective layer over SS310. This is due to the lower chromium content in N350 than SS310, which the volatilization more clearly in SS310 than N350.

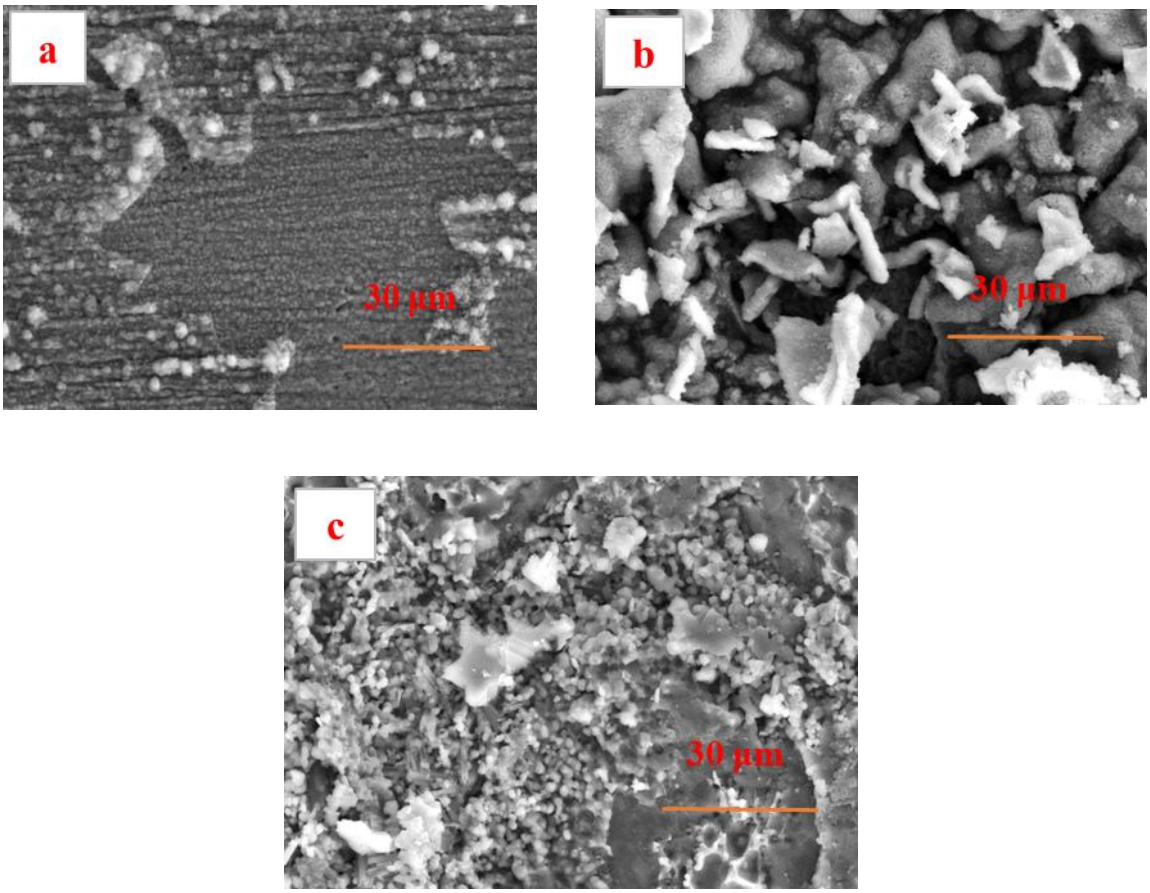

Fig. 16. The SEM micrographs of the oxidized surface of SS310 for 50 h in dry air (a) 850 °C, (b) 950 °C, and (c) 1050 °C.

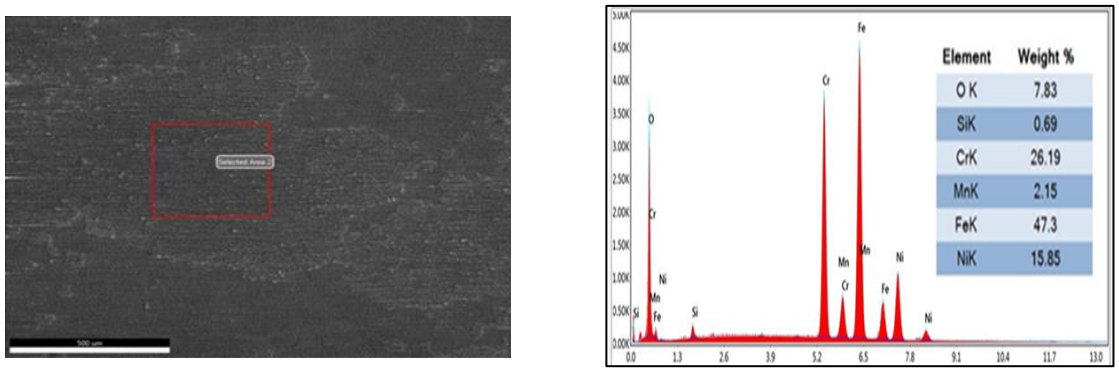

(a)

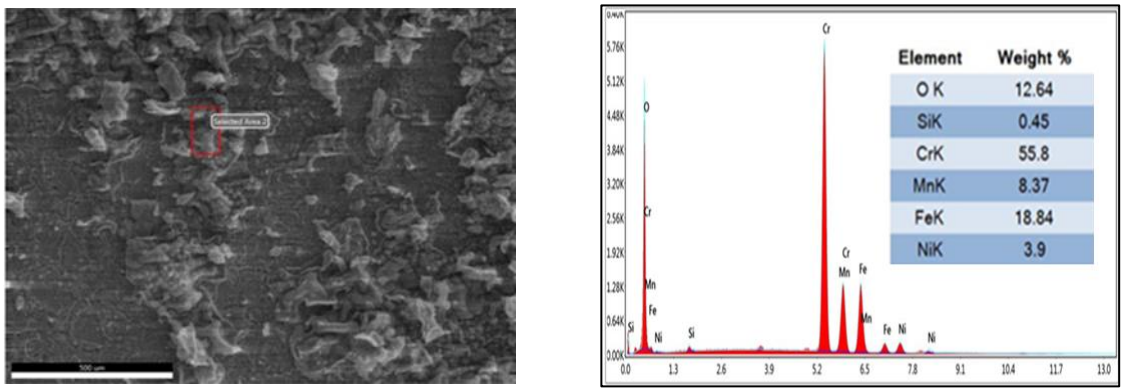

(b)

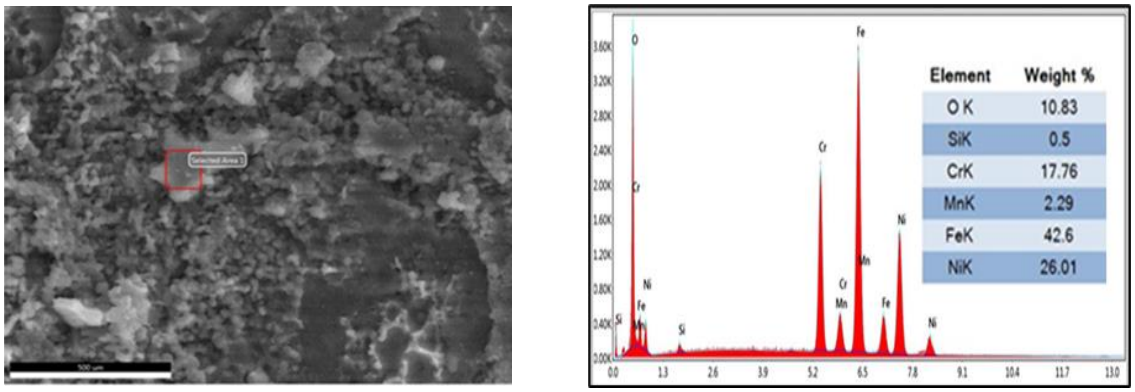

(c)

Fig. 17. The SEM micrographs and EDX analyses of the oxidized surface of SS310 for 50 h in dry air (a) 850 °C, (b) 950 °C, and (c) 1050 °C

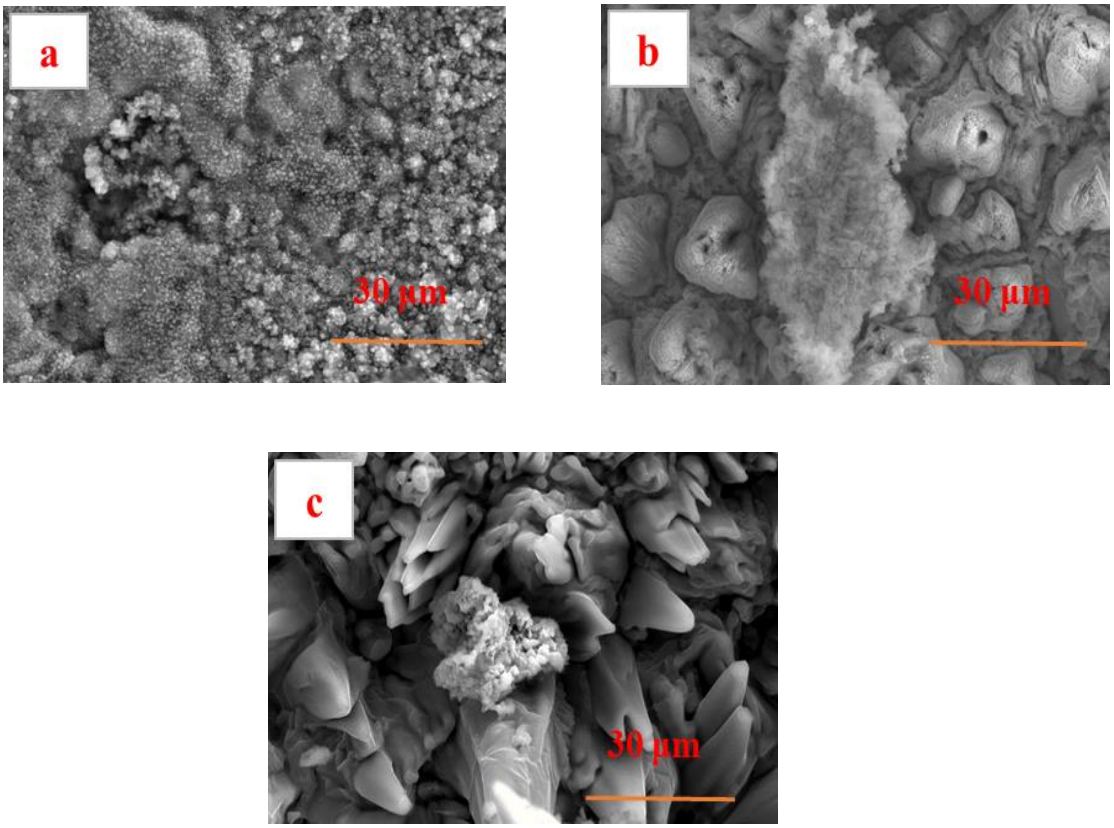

Fig. 18. The SEM micrographs of the oxidized surface of N350 for 50 h in dry air (a) 850 °C, (b) 950 °C, and (c) 1050 °C

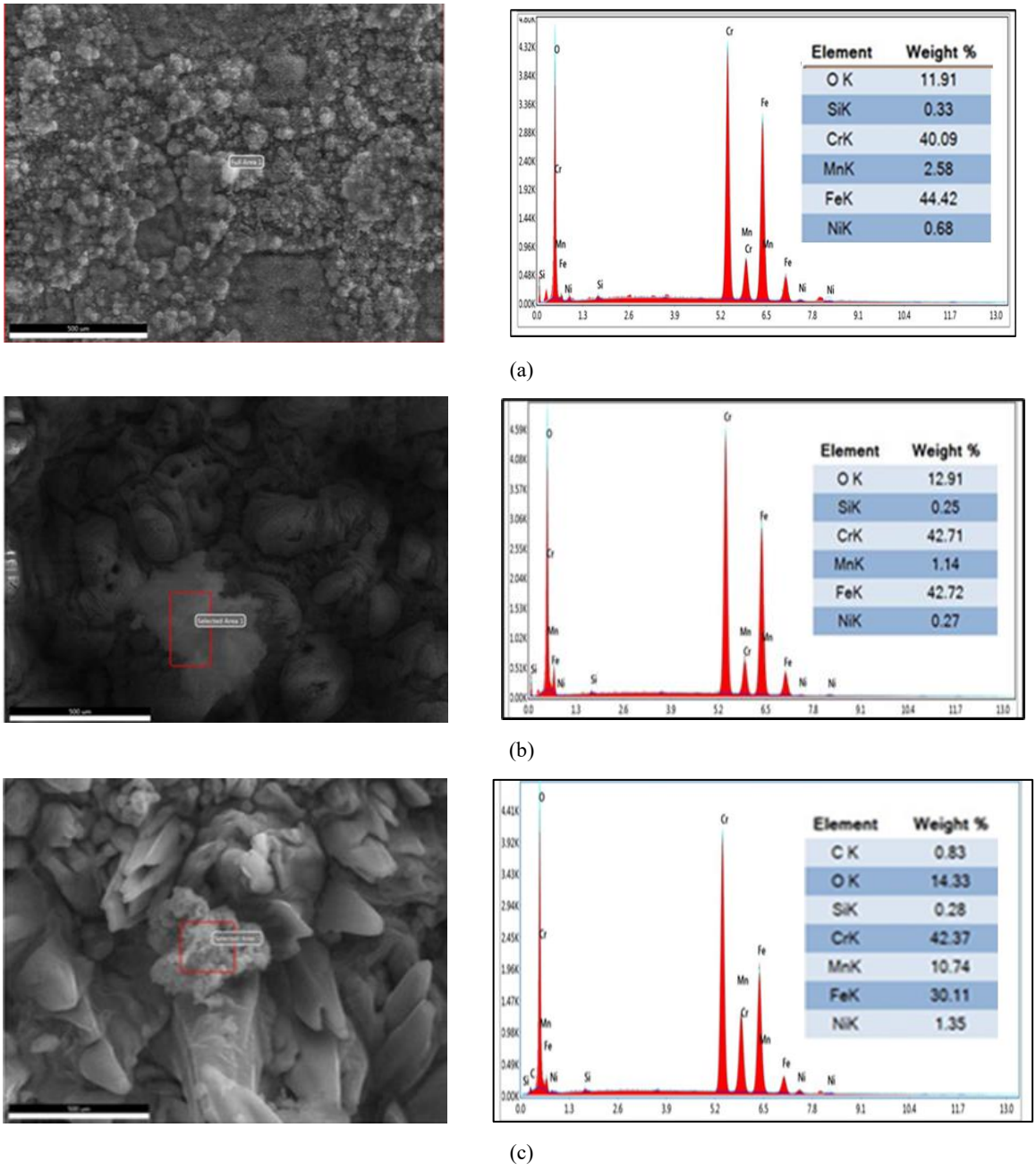

Fig. 19. The SEM micrographs and EDX analyses of the oxidized surface of N350 for 50 h in dry air (a) 850 °C, (b) 950 °C, and (c) 1050 °C

Conclusions

The characterizations of the SS310 and N350 were examined. The oxidation behavior of SS310 and N350 was conducted at temperatures of 850°C, 950°C, and 1050°C for 50 h in dry air. The following conclusions were drawn:

- The microstructure of N350 shows bainite and retained austenite structure, whereas SS310 shows the austenitic structure with a small amount of ferrite.
- The N350's phase identification has two phases: ferrite and austenite, whereas the SS310 has only one phase (austenite).
- The hardness value of N350 (419 HV) is nearly twice that of SS310 (202 HV), while the Young's modulus value of N350 (220 Gpa) is greater than that of SS 310 (194 Gpa).

- The oxidation follows a parabolic law for SS310 and N350 in the temperature range 850 ~ 1050 °C for 50 h in dry air. The parabolic rate constant values of SS310 are $3.00x10^{-9}$ $g^2/(cm^4 \cdot h)$, $2.00x10^{-8}$ $g^2/(cm^4 \cdot h)$, $2.00x10^{-6}$ $g^2/(cm^4 \cdot h)$ for 850 °C, 950 °C, and 1050 °C, respectively. While the parabolic constants of N350 are $7.00x10^{-9}$ $g^2/(cm^4 \cdot h)$, $9.00x10^{-6}$ $g^2/(cm^4 \cdot h)$, and $2.00x10^{-5}$ $g^2/(cm^4 \cdot h)$ for 850 °C, 950 °C, and 1050 °C, respectively. The oxidation rate values increase with increased oxidation temperature for both SS310 and N350. This could potentially be attributed to the increasing Cr content in SS310, which maintains a protective layer of Cr_2O_3 up to 1000 °C before becoming volatile and reducing its oxidation resistance. This phenomenon was more evident in SS310 compared to N350, likely due to the higher Cr content in SS310.
- The activation energy of N350 (217.6 KJ/mol) is higher than that of SS310 (172.05 KJ/mol). Thus, the oxidation resistance of N350 is higher than SS310.

Declaration of Competing Interest

There are no conflicts to declare.

Acknowledgments

Emad El-Kashif, Lamiaa Z. Mohamed, and Esraa Kamal acknowledge the support from the Faculty of Engineering, Cairo University, and Sanaa S. Abd Elmomen would like to acknowledge the support from the Tabbin Institute for Metallurgical Studies.

References

[1]. W. Ming, Z. Chen, J. Du, Z. Zhang, G. Zhang, W. He, J. Ma, F. Shen, A comprehensive review of theory and technology of glass molding process, The International Journal of Advanced Manufacturing Technology, 107(2), 2020

[2]. K. Li, Y. Zeng, J-L. Luo, Corrosion of SS310 and Alloy 740 in high temperature supercritical CO2 with impurities H2O and O2, Corrosion Science 184 (2021) 109350

[3]. D.S. Kumar, P. Srikar, A Review on Comparison of Mechanical Properties of Dissimilar Steels Welded by TIG and MIG, E3S Web of Conferences, 184, 01030(2020)

[4]. B. Naik, A.C. Reddy, Optimization of tensile strength in TIG welding using the Taguchi method and analysis of variance (ANOVA), Thermal Science and Engineering Progress, 8, 327-339.(2018)

[5]. M.B. Leban, M. Vončina, T. Kosec, R. Tisu, M. Barborič, J. Medved, Comparison of Cycling High Temperature Corrosion at 650°C in the Presence of NaCl of Various Austenitic Stainless Steels, Oxidation of Metals (2023) 99:63–77.

[6]. L. Dong-sheng, L. Dan, D. Hong, G. Pei, L. Yu, X. Chen, X. Jiang, P. Jing-Juan, High-temperature oxidation resistance of austenitic stainless steels, Key Engineering Materials, 575-576, 414-417, 2014

[7]. M.K. Jiang, Y. Han, T. Zhang, Microstructural characterization of aging precipitation behavior of 17Cr-0.86Si-1.2Cu-0.5Nb ferritic stainless steel, Materials Characterization 171 (2020) 110779

[8]. L. Gan, X. Montero, S.A. Sheikh, Microstructure and area specific resistance of cathodic half cells for solid oxide fuel cells composed of perovskite-type cathodes and Co-alloy-coated ferritic stainless steel interconnects, Surface and Coatings Technology 406 (2020) 126659

[9]. L. Wei, J.H. Zheng, L.Q. Chen, Interrelationship between Deformation Parameters and Fracture Mechanisms in Gradient Nanostructured Stainless Steel, Corrosion Science 142 (2018) 79–92

[10]. Z. Wang, C. Li, X.Q. Si, Oxidation behavior of ferritic stainless steel interconnect coated by a simple diffusion bonded cobalt protective layer for solid oxide fuel cells, Corrosion Science 172 (2020) 108739

[11]. P.N. Vicente, A.N. Galindo, J.F.A. Bello, Analysis of oxide scales on oxidised EN 1.4509 ferritic stainless steel catalyst support by scanning electron microscopy, IOP Conference Series Materials Science and Engineering 891 (2020) 012017

[12]. X. Jiang, X. Che, Z. Zhang, S. Yin, H. Wang, L. Chen, High temperature oxidation behavior and mechanism of FeXCr0.5Ti ferritic stainless steels, Mater. Res. Express 8 (2021) 046511

[13]. S. Aghaeian, F. Nourouzi, W.G. Sloof, J.M.C. Mol, A.J. Böttger, Predicting the parabolic growth rate constant for high-temperature oxidation of steels using machine learning models, Corrosion Science 221 (2023) 111309.

[14]. L. Cheng, B. Sun, C. Du, W. Gao, G. Cao, High-Temperature Oxidation Behavior of Fe–10Cr Steel under Different Atmospheres, Materials 2021, 14, 3453.

[15]. Z. Li, Evolution Mechanism of Oxide Scale of Hot Rolled Steel and Development of Acid-Free Picking Technology; Northeast University: Shenyang, China, 2018.

[16]. M.S. Li, High Temperature Corrosion of Metals; Metallurgical Industry Press: Beijing, China, 2001; 247–248.

[17]. K. Chen, L. Zhang, Z. Shen, X. Zeng, Revealing the oxidation mechanism of 310S stainless steel in supercritical water via high-resolution characterization, Corrosion Science 200 (2022) 110212.
[18]. Y. Behnamian, A. Mostafaei, A. Kohandehghan, B.S. Amirkhiz, D. Serate, W. Zheng, D. Guzonas, M. Chmielus, W. Chen, J.L. Luo, Characterization of oxide scales grown on alloy 310S stainless steel after long term exposure to supercritical water at 500 ◦C, Mater. Charact. 120 (2016) 273–284.
[19]. A.C.S. Sabioni, A-M. Huntz, E.C. da Luz, M. Mantel, C. Haut, Comparative Study of High Temperature Oxidation Behaviour in AISI 304 and AISI 439 Stainless Steels, Materials Research, 6(2) (2003) 179-185.
[20]. T. Zheng, J. Han, High temperature oxidation behavior of SUS310S austenitic stainless steel, Advanced Materials Research. 941-944 (2014) 212-215.
[21]. R. El-Mallawany, H. Afifi, Elastic moduli and crosslinking of some tellurite glass systems. Materials Chemistry and Physics. 143, 2013.
[22]. L.Z. Mohamed, S. S. Abd Elmomen, S. El-Hadad, Influence of the oxidation behavior of Ti–6Al–4V alloy in dry air on the oxide layer microstructure, Chemical Papers (2022) 76:1627–1638
[23]. L.Z. Mohamed, S.S. Abd Elmomen, S. El-Hadad, Investigating the thermal oxidation behavior of Ti–6Al–7Nb alloy in dry air, Materials and Corrosion. 2022; 73: 1553–1562.
[24]. A.E. Tudose, I. Demetrescu, F. Golgovici, M. Fulger, Oxidation Behavior of an Austenitic Steel (Fe, Cr and Ni), the 310 H, in a Deaerated Supercritical Water Static System, Metals 2021, 11, 571.
[25]. L.Z. Mohamed, S.S. Abd ElMoamen, S.J. Yoo, M.A-H. Gepreel, Oxidation of Fe35Mn21Ni20Cr12Al12 High Entropy Alloy in Dry Air, Alloys 2024, 3, 43-58.
[26]. V. Higuera-Hidalgo, F. J. Belzunce-Varela, J. Riba-López, High temperature ciclyc oxidation of AISI 310 steel in atmospheres with variable oxidation content, Rev. Metal. Madrid, 41(3) (2005) 204-2011.
[27]. R. Yin, Carburization of 310 stainless steel exposed at 800–1100 °C in 2%CH4/H2 gas mixture, Corrosion Science 47 (2005) 1896–1910.
[28]. I.C. García, A.N. Galindo, J.F.A. Bello, J.M.G. Leal, J.F.B. Pedemonte, Characterisation of High Temperature Oxidation Phenomena during AISI 430 Stainless Steel Manufacturing under a Controlled H2 Atmosphere for Bright Annealing, Metals 2021, 11, 191.
[29]. C.E.R. de Carvalho, G.M. da Costa, A.B. Cota, E.H. Rossi, High Temperature Oxidation Behavior of AISI 304 and AISI 430 Stainless Steels, Materials Research, 9(4), 393-397, 2006.
[30]. J.G.d.C. Passos, D. Silva, R.B.D. Pereira, A.M.d.S. Malafaia, Influence of test parameters on the cyclic oxidation behavior of AISI 310 and a new Fe-5.9Si-3.9Cr-4.5Ni-0.8C (wt.%) alloy, revista Matéria, 27(3), 2022.